Journal of Advances in Science and Technology
Vol. 22, Issue No. 2, April-2025, ISSN 2230-9659

DOI: https://doi.org/10.29070/n61tch90

Optical and morphological investigation of $Y_2O_3:Tb^{3+}$ (1 mol%) and Bi^{3+} co-doped $Y_2O_3:Tb^{3+}$ (1 mol%) nanoparticles

Renu [1] * , Dr. Heena Dahiya [2] , Dr Jitender Jindal [3] , Dr. Nitika Mor [4]

1. Research Scholar, Baba Mastnath University- Asthal Bohar, Rohtak, Haryana, India renutundwal5@gmail.com ,
2. Assistant Professor, Department of Physical Sciences (Chemistry), Baba Mastnath University- Asthal Bohar Rohtak, Haryana, India ,
3. Assistant Professor, Department of Chemistry, RPS Degree College, Balana, Mahendergarh, Haryana, India ,
4. Assistant Professor, Department of Physical Sciences (Chemistry), Baba Mastnath University- Asthal Bohar Rohtak, Haryana, India

Abstract: $Y_2O_3:Tb^{3+}$ (1 mol%) and Bi^{3+} co-doped $Y_2O_3:Tb^{3+}$ nanophosphors were synthesized via combustion method at 1000 °C. The synthesized samples were characterized using a number of techniques, including XRD, SEM, EDX, Elemental mapping, PL, and XPS. XRD and SEM for structural and morphological characterization, which verified phase purity and homogeneous morphology. According to photo-luminescence research, the $4f^6\ 5d^1 \rightarrow 4f^7$ transition of Tb^{3+} is responsible for the broad excitation at 324 nm and the noticeable blue emission at 465 nm. Bi^{3+} and ions were successfully incorporated into the Y_2O_3 lattice, as confirmed by XPS, both of which maintained their trivalent oxidation states with little discernible distortion. These results demonstrate effective co-doping and imply improved luminescence through energy transfer processes with very small concentrations of rare-earth element.

Keywords: Nanophosphors, solution-combustion method, XRD, SEM, XPS

X

INTRODUCTION

Overview, in recent years, rare-earth doped nanophosphors have attracted a lot of attention because of their exceptional optical qualities and possible uses in sensors, solid-state lighting, and display technologies. Because of its great thermal stability, wide bandgap, low phonon energy, and exceptional chemical durability, yttrium oxide (Y_2O_3) is regarded as an outstanding host material among several host lattices [1]. In addition, yttrium oxide, a type of rare earth oxide, is crucial for a range of photonic applications. As a host material, yttrium oxide is widely used in fluorescent lamps, lasers, plasma display panels, sensing devices, cathode ray tubes, various detection devices, and field emission displays. Y^{3+} shares similar ionic radii and chemical characteristics with other rare earth ions, making yttrium oxide an effective host material for these ions. When doped with rare earth ions, yttrium oxides exhibit impressive luminescent properties, including prolonged luminescent decay times and narrow emission lines. These attributes make yttrium oxide particularly appealing for use in optical communication, display technologies, and solar cells. We improved the rare earth emissions in doped yttrium oxide through co-doping with some sensitizers along with rare earth ions, which is of significant interest due to the potential for non-radiative energy transfer [2-4].The addition of Bi^{3+} enhances the photoluminescence intensity of Tb^{3+}, even in lower amounts.

Furthermore, Bi^{3+} doping can slightly alter the structural parameters of Y_2O_3 nano-particles as Bi^{3+} has a slightly larger ionic radius (Bi^{3+}: 1.03 Å compared to Y^{3+}: 0.90 Å), its substitution leads to local lattice distortions, which may create conditions that promote luminescence and affect defect-related non-radiative centers [5, 6]. This capability is useful for creating tailored nanophosphors suitable for a range of optoelectronic and bioimaging applications [7]. Additionally, Y_2O_3:Tb^{3+} phosphors are characterized by their excellent thermal and chemical stability, extended lifespans, and high quantum efficiency qualities that are critical for use in advanced optoelectronic applications like field emission displays and white LEDs [8]. Recent progress in nanotechnology has facilitated the creation of Y_2O_3:Tb^{3+} nanophosphors, which enhance performance in biomedical imaging owing to their small size and compatibility with biological systems [9].

Doping Y_2O_3 nanoparticles with Bi^{3+} can affect their morphology, grain size, and surface defect states, typically resulting in improved crystallinity and decreased non-radiative losses [10]. Terbium (Tb^{3+}) is the main activator ion in Y_3O_3:Tb^{3+}, Bi^{3+} nanophosphors, a type of luminous materials that generate bright green light because of the $^5D_4 \rightarrow {}^7F_J$ transitions, especially at ~545 nm. By absorbing excitation energy (often in the near-UV range) and effectively transferring it to Tb^{3+} ions, the use of bismuth (Bi^{3+}) as a sensitiser improves the photoluminescence efficiency and increases the intensity of green emission[11,12]. By increasing surface area, reducing light scattering, and producing quantum confinement effects, doping both Tb^{3+} and Bi^{3+} into the Y_2O_3 matrix at the nanoscale can increase luminous characteristics, making these nanophosphors appropriate for high-resolution displays and cutting-edge optical devices [13]. Furthermore, the crystal field environment can be influenced by Bi^{3+} co-doping, which may adjust emission properties [14].

This research involved the synthesis of a Y_2O_3:Tb^{3+} and Bi^{3+} co-doped Y_2O_3:Tb^{3+} nano-phosphors using combustion methods. The phosphor was analyzed through techniques including X-ray diffraction (XRD), X-ray Photoelectron Spectroscopy (XPS),Scanning electron microscopy (SEM) with Energy Dispersive X-ray spectroscopy (EDX), and Photo-luminescence (PL).

SYNTHESIS AND CHARACTERIZATION

Synthesizes of Y_2O_3: Tb^{3+} nano-phosphors

Y_2O_3 nano phosphors doped with 1 mol % Tb^{3+} were produced using a solution combustion method, which is a wet-chemical process. This approach requires both a fuel and an oxidizer. In the combustion process, metal nitrates serve as the oxidizing agent, while urea acts as the reducing agent. The proportions of yttrium nitrate, terbium nitrate, and urea are determined by the overall oxidizing and reducing valencies of the oxidizer and fuel [15-16]. Yttrium oxide nanophosphors doped with terbium were created by combining yttrium nitrate [$Y(NO_3)_3 \cdot XH2O$], terbium nitrate [$Tb(NO_3)_3 \cdot 6H_2O$], and urea [$CO(NH_2)_2$] in double-distilled water. The chemicals were blended according to their stoichiometric ratios to produce a uniform solution. This solution was then placed in a silica crucible and heated in a preheated muffle furnace at a consistent temperature of 600°C for 15 minutes. Following the combustion process, the resulting sample was foamy, which was then crushed into a fine powder and further calcined at 1000°C. This powder was subsequently collected for analysis and characterization.

Synthesizes of Bi^{3+} co-doped $Y_2O_3:Tb^{3+}$ nano-phosphors

By using the solution combustion approach, Tb^{3+}-doped (1 mol %) and Bi^{3+}codoped (1 mol %) Y_2O_3 nanophosphor were created. By combining yttrium nitrate [$Y(NO_3)_3.XH_2O$], terbium nitrate [$Tb(NO_3)_3.6H_2O$], bismuth nitrate pentahydrate, and urea [$CO(NH_2)_2$] in double-distilled water, terbium doped, Bi co-doped Y_2O_3 nanophosphor was created. A homogenous solution was created by mixing all the components in a stoichiometric ratio. The homogeneous solution in the silica crucible was held at 600°C for 15° minutes in a muffle furnace that had been warmed. The sample was foamy when the combustion process was finished, the resulting frothy sample was easily pulverised into a fine precursor powder using an agate mortar. In order to attain better crystallinity, it was also annealed for two hours at 1000 °C. The sample was also safely kept in a desiccator for different characterisations.

Materials Characterization

The Multipurpose Versatile XRD System (Smart Lab 3kW, Rigaku) was utilized for powder XRD and thin film XRD analysis of Bi^{3+} ions co-doped with $Y_2O_3:Eu^{3+}$ phosphor samples, covering a 2θ range from 10º to 70º, to assess the structure and phase purity. The surface morphology of the $Y_2O_3:Tb^{3+}$ and Bi^{3+} activated phosphor samples was examined with a High-Resolution Field Emission Scanning Electron Microscope with EDS (FE-SEM) (JSM-7610F Plus, JEOL) Luminescence decay profiles for the $Y_2O_3:Tb^{3+}$, Bi^{3+} samples were recorded using a Quanta Master 8450-22 Spectrofluorometer (Horiba), capable of measuring fluorescence across the UV-VIS-NIR range (~200 nm to 3000 nm). X-ray photoelectron spectroscopy (XPS, AXIS Supra) was employed to analyze the chemical bonding configurations.

RESULTS AND DISCUSSION

Structural Analysis

XRD

Figure 1 presents the X-ray diffraction patterns of $Y_2O_3:Tb^{3+}$ (1mol %), and $Y_2O_3:Tb^{3+}$ (1mol %), Bi^{3+} (1 mol %) nanophosphors, which were calcined at 1000 °C. The results show that, when compared to the standard JCPDS data, there are no observable impurity peaks in the XRD patterns. This indicates that the synthesized samples are single-phase and that the trivalent terbium and bismuth ions have successfully incorporated into the Y_2O_3 host without changing the crystal structure.

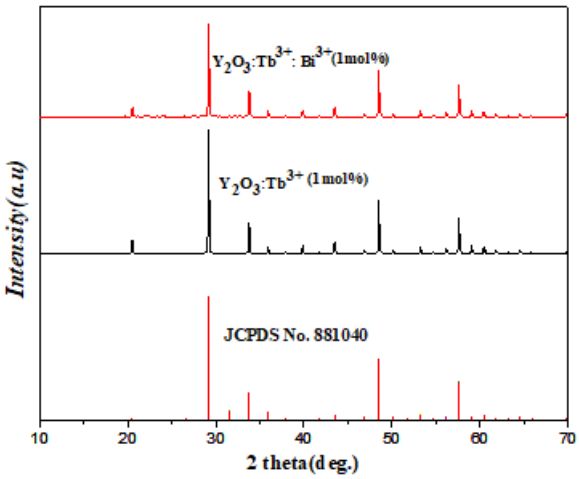

Figure 1: Displays the powder X-ray diffractograms for the pure host and the $Y_3O_3:Tb^{3+}$, Bi^{3+} samples, as well as the standard JCPDS data for the Y_2O_3 host.

Assessment of structural parameters

XRD data was used to determine the structural characteristics, including crystallite size, dislocation density, and microstrain. As stated below, the Debye-Scherrer's formula (1) [17] and the Hall-Williamsons equation (2) [18] were used to calculate the crystallite size (D).

$$D = \frac{0.9\lambda}{\beta \cos\theta}$$ (Debye – Scherrer Formula) (1)

$$\frac{\beta \cos\theta}{\lambda} = \frac{1}{D} + \frac{\epsilon \sin\theta}{\lambda}$$ (Hall – Williamsons equation) (2)

Here, the microstrain in the samples is denoted by ε, and the full-width at half-maximum (FWHM) is represented by β. The following relations (3), (4) [19] were used to compute the dislocation density (δ), and microstrain (ε).

$$\delta = \frac{1}{D^2} \quad (3)$$

$$\varepsilon = \frac{\beta \cos\theta}{4} \quad (4)$$

The structural characteristics of the $Y_2O_3:Tb^{3+}$ (1mol %) and $Y_2O_3:Tb^{3+}$ (1mol %), Bi^{3+} (1mol %) nanophosphors are compiled in Table 1.

Samples	Crystallite size (nm)	Strain (ε)	FWHM (2θ in degree)	Dislocation density (δ)
$Y_2O_3:Tb^{3+}$	61.2641606	8.985052824	0.13107	2.66432E-07
$Y_2O_3:Tb^{3+}$, Bi^{3+}	58.39364835	9.423285268	0.13751	2.93271E-07

Scanning electron microscopy (SEM) and Energy Dispersive X-ray spectroscopy (EDS)

Morphological studies

The surface morphology and crystallite sizes of the synthesised phosphor powder were further examined using a scanning electron microscope. Figure 2a–b displays SEM micrographs of $Y_2O_3:Tb^{3+}$, Bi^{3+} phosphor materials along with morphological pictures. It is quite evident from the SEM micro-graph that the sizes of the nanoparticles ranges from 80 to 100 mm and are spherical in shape. According to SEM pictures, all of the created compositions have almost identical crystallization which confirms the homogeneity and formation of single phase.

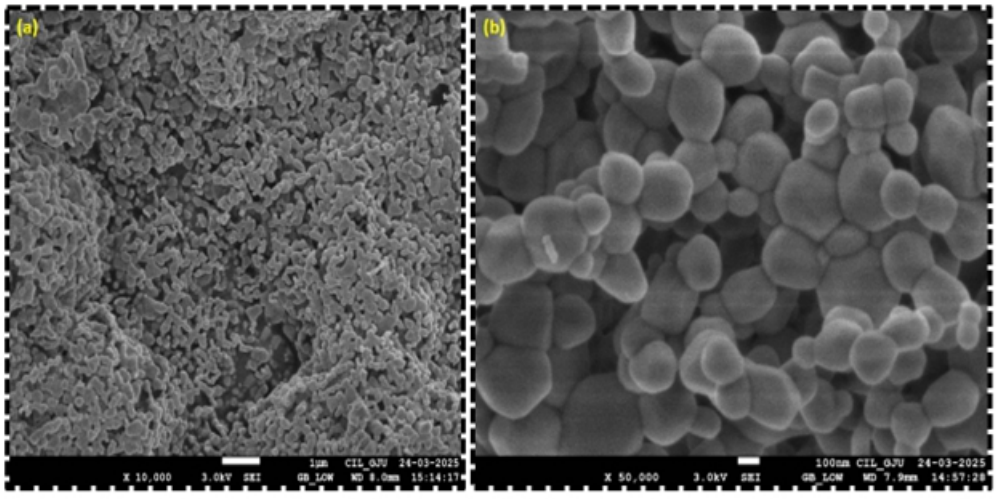

Figure 2 (a–b). Shown SEM morphology of $Y_2O_3:Tb^{3+}$, Bi^{3+} phosphor at various magnifications.

Elemental analysis

Moreover, High-Resolution Field Emission Scanning Electron Microscope with EDS (FE-SEM) (JSM-7610F Plus, JEOL) was used to evaluate the elements and its composition of the bismuth doped prepared phosphors. Figure 3 displays FE-SEM-EDS images of sample with 1.0 weight% of Tb and 5 wt % Bi co-doped Y_2O_3. The spectra distinctly show that the samples contained only terbium (Tb), bismuth (Bi), oxygen (O), and yttrium (Y), with no other impurities detected. These peaks show that the synthesized phosphors contain composite components. The inset of Figure 3 lists the spectra of the region of the characterized phosphor that is being considered as well as the atomic percentage of the original reactant

components.

The homogeneous distribution of elements across the whole particle range is further demonstrated by the elemental mapping displayed in Fig. 4(a–e), with yttrium and oxygen elements exhibiting comparatively higher concentration content.

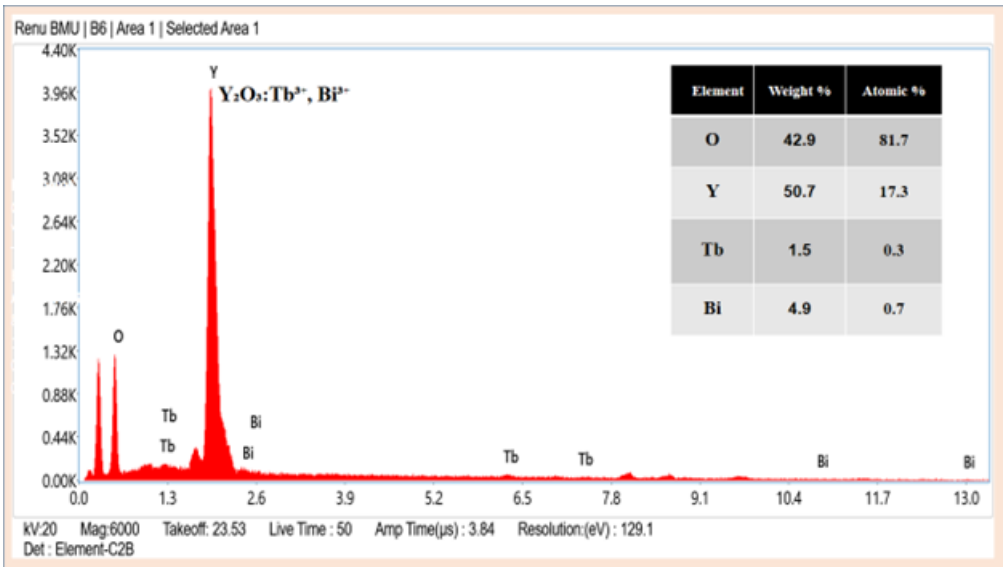

Figure 3. Energy dispersive spectroscopy and field emission scanning electron microscopy images of Tb and Bi doped Y_2O_3 nanophosphors.

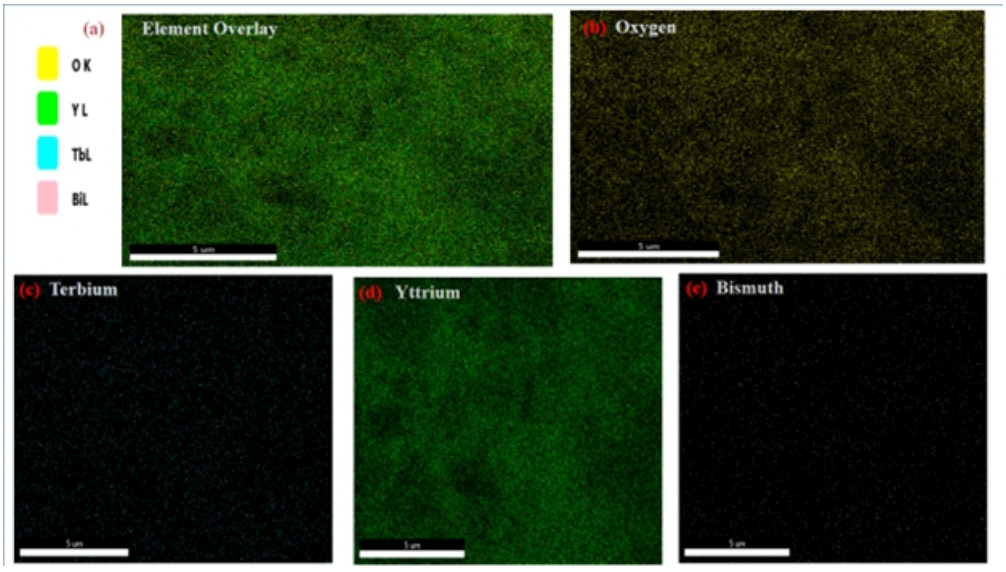

Figure 4. Y_2O_3:Tb^{3+}, Bi^{3+} nanophosphor calcined at 1000 °C (a) Element overlay, (b) Oxygen, (c) Terbium, (d) Yttrium, and (e) Bismuth elements.

Photoluminescnce (PL) Analysis:

The PL excitation and emission spectra were recorded for both Y_2O_3 doped with Tb^{3+} (1 mol %) shown in Fig. 5(a-b) and with co-doped Bi^{3+} in Fig. 6(a-b). Firstly, in Fig 5 (a), the excitation spectrum recorded at

545 nm emission, which shows a broad band ranging from 300 to 338 nm that corresponds to the intra-configurational transition from the ground state $^7F_6$ of the $4f^8$ configuration to the $4f^75d^1$ configuration of Tb^{3+} and the highest peak is observed at 307 nm associated with O^{2-} - Tb^{3+} charge transfer centers.

Whereas, in Fig 5 (b) the excitation maxima occurring at 307 nm which is attributed to the $^1S_0 \rightarrow {}^3P_1$ transition of Bi^{3+} ion and a shoulder around 290 nm is correspondent to the $4f^8 \rightarrow 4f^75d^1$ transition of Tb^{3+} ion. The excitation efficiency is enhanced throughout the spectral range from 300 to 400 nm as compared with the excitation spectrum of Y_2O_3:Tb^{3+}. In Fig 5(b), the emission spectra of Y_2O_3:Tb^{3+} observed at 307 nm and according to that the transitions takes place from ^5D_J levels to ground state of Tb^{3+} ions, giving rise to sharp line emissions. The emission below 480 nm originates from $^5D_3 \rightarrow {}^7F_J$ transition and above 480 nm originates from $^5D_4 \rightarrow {}^7F_J$ transition of Tb^{3+} ions. It exhibit broad emission lines located at 484 nm, 490 nm, 544 nm, 551 nm. All these emissions are originates from $^5D_4 \rightarrow {}^7F_j$ transitions and the emission corresponds to $^5D_3 \rightarrow {}^7F_J$ was not observed in this case. The peaks at 484-490 nm are attributed to $^5D_4 \rightarrow {}^7F_6$ transition which is forced electric dipole allowed transition whereas the emission peaks at 544-551 nm are attributed to $^5D_4 \rightarrow {}^7F_5$ transition of Tb^{3+} ions which is magnetic dipole allowed [20-22]. The dominant and most intense emission occurs at 544 nm responsible for the green light. In Fig 6 (b), Under the 307 nm, it exhibit broad emission lines located between 484-551 nm. But here also some small peaks appeared at 583 and 596 corresponding to $^5D_4 \rightarrow {}^7F_4$ and at 613 and 628 nm corresponding to $^5D_4 \rightarrow {}^7F_3$. Overall, the the new peak appeared in Fig. 6 (a) indicates that the energy is transferred from $^3P_1$ level of Bi^{3+} ion to the $^5D_4$ level of Tb^{3+} ion. In this case, Bi^{3+} ions absorb radiation and, subsequently energy is transferred from Bi^{3+} ions to Tb^{3+} ions and emits light via $^5D_4 \rightarrow {}^7F_j$ transitions [23]. The energy transfer mechanism, where Bi^{3+} ion acts as a 'sensitizer' for Tb^{3+} emission is presented in Fig 7. (Schematic diagram).

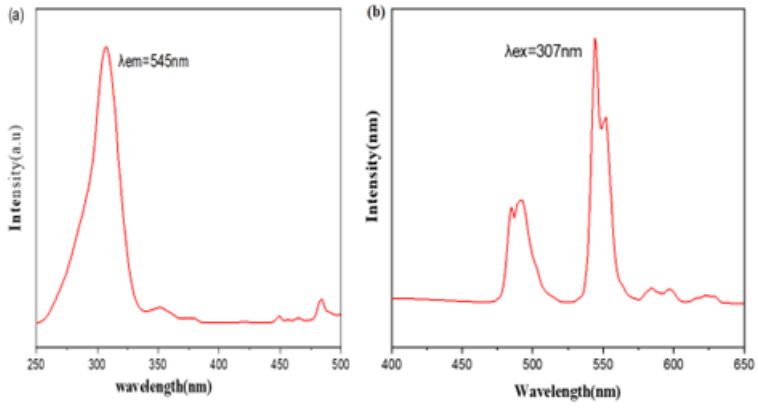

Figure 5 (a) The excitation spectrum of Y_2O_3:Tb^{3+} nanoparticles (NPs) measured at an emission wavelength of 545 nm. (b) The emission spectra measured with an excitation wavelength of 307 nm.

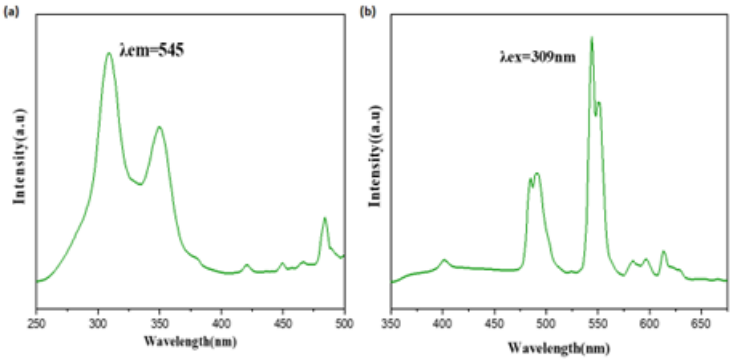

Figure 6 (a) The excitation spectrum for $Y_2O_3:Tb^{3+}$, Bi^{3+} nanoparticles (NPs) recorded at an emission wavelength of 545 nm. (b) The emission spectra obtained using an excitation wavelength of 309 nm.

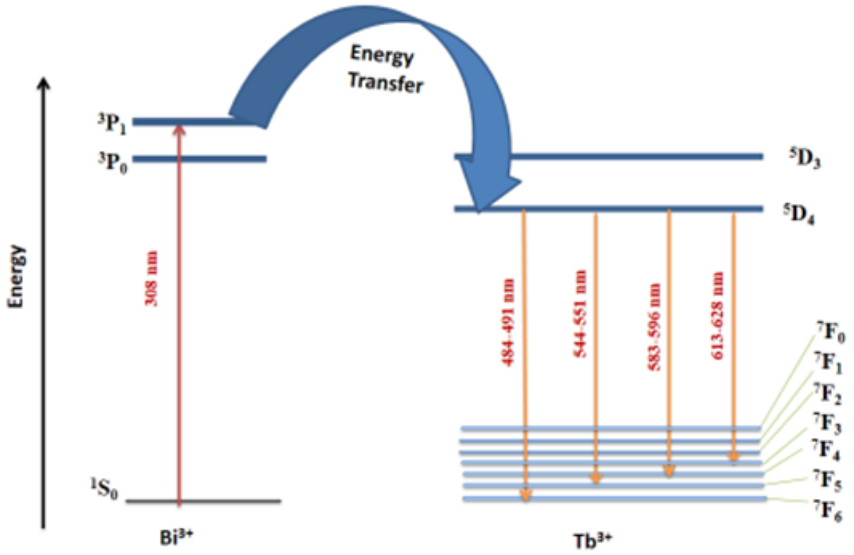

Figure 7: Schematic Energy transfer mechanism in Bi^{3+} ions for $Y_2O_3:Tb^{3+}$ nanophosphor.

Calculation of CIE parameters

The analysis of CIE coordinates, and correlated color temperature (CCT) was conducted for $Y_2O_3:Tb^{3+}$ and Bi^{3+} co-doped $Y_2O_3:Tb^{3+}$ phosphors. Fig. 8 shows the evaluation of the CIE coordinates and the resulting color. The nature of colour emission was examined by computing the Correlated Color Temperatures (CCT). CCT was calculated using the following McCamy empirical formula (5).

$$CCT = -449n^3 + 3625n^2 - 6823.3n + 5520.33 \quad (5)$$

Where $x_e = 0.3320$ and $y_e = 0.1858.6$ and n is the ratio of $(x-x_e)$ and $(y-y_e)$ [24, 25]. Figure 9. Presents the CCT graphs for $Y_2O_3:Tb^{3+}$ (1mol %) and Bi^{3+} (1mol %) co-doped $Y_2O_3:Tb^{3+}$ (1mol %) , with the CCT values for the phosphor. The CCT values range from 6689 to 6875K, As a result, the CCT values for

all the prepared samples indicate a warm light emission. Table 2 lists the calculated CIE coordinates and CCT values.

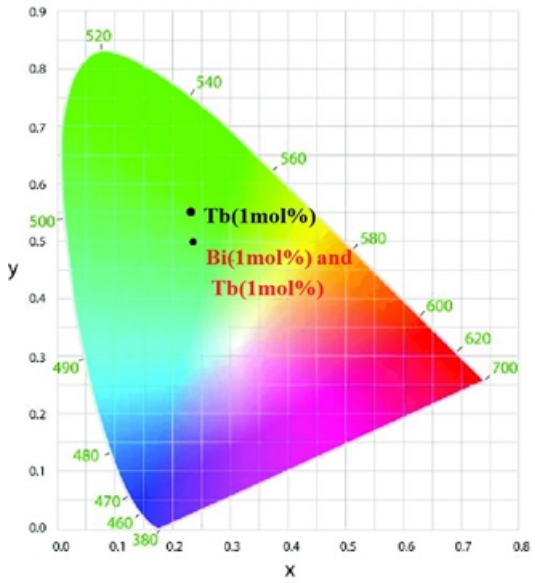

Figure 8. (a) Presents the CIE coordinates for $Y_2O_3:Tb^{3+}$ and $Y_2O_3:Tb^{3+}$, Bi^{3+}.

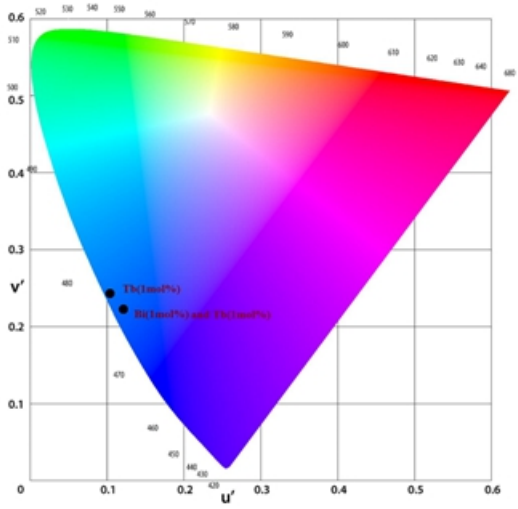

Figure 9. Diagram of u' and v' for $Y_2O_3:Tb^{3+}$and $Y_2O_3:Tb^{3+}$, Bi^{3+}.

Table 2. CIE, u' and v' and CCT data for $Y_2O_3:Tb^{3+}$and $Y_2O_3:Tb^{3+}$, Bi^{3+}.

Sample	CIE	(u', v')	CCT (K)
$Y_2O_3:Tb^{3+}$	(0.273455,0.557452)	(0.119641,0.243894)	6689
$Y_2O_3:Tb^{3+}$, Bi^{3+}	(0.277308,0.488837)	(0.133459,0.23526)	6875

XPS analysis

The chemical composition of the Y_2O_3:Tb^{3+}, Bi^{3+} nanocomposite is determined using X-ray photoelectron spectroscopy (XPS). The XPS survey produced from Y_2O_3 is shown in the Figure 10. The Tb^{3+}, Bi^{3+} nanocomposite forms the O(1s), Bi(4f), Y(3d), C(1s), and Tb(4d) peaks. The high resolution peaks of the O(1s) spectra at 525.1 eV and 527.8 eV, which correlate to the regular Y-O bond of the Y_2O_3 nanoparticles [26]. The high resolution peak of the C(1s) spectra at 281 eV and 296 eV. The peak at 308 eV represents the Y (3p) spectra. The sharp peak observed in the high-resolution Y (3d) spectra occurs at 160.9 eV, while the peak at 165.5 eV is attributed to the Bi (4f) of the sample. Additionally, the peaks at 153.02 eV and 155.08 eV represent a doublet for Tb (4d), resulting from spin-orbit coupling [27-28].

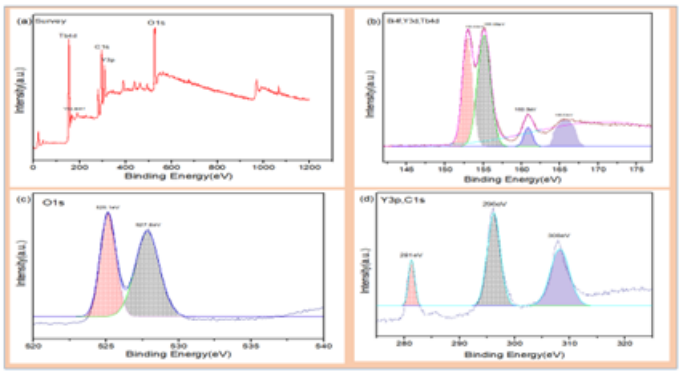

Figure 10. High-resolution XPS spectra for the (a) survey, (b) Bi4f, Y3d, Tb4d, (c) O 1s and (d) Y 3p, C1s peaks.

CONCLUSIONS

In conclusion, Y_2O_3:Tb^{3+} and Bi^{3+} co-doped Y_2O_3:Tb^{3+} nano-phosphors emitting green light was synthesized using a urea-assisted solution-combustion technique. The produced phosphor's phase purity was validated by XRD. Successful nanophosphor production was indicated by the consistently dispersed, primarily spherical crystallizes between 80 and 120 nm that were found by SEM analysis. Co-doping did not significantly impact the morphology, indicating that the inclusion of Bi^{3+} and Tb^{3+} does not change the microstructure. The elemental composition was further confirmed by EDS analysis, which supported efficient dopant integration without phase separation and confirmed the existence of Yttrium, Oxygen, Terbium, and Bismuth. Green emission is seen in the PL excitation spectra of Y_2O_3:Tb^{3+} from $^5D_4 \rightarrow {}^7F_J$ transitions. The $^1S_0 \rightarrow {}^3P_1$ transition of Bi^{3+} causes extra greem emission in Bi^{3+} co-doped Y_2O_3: Tb^{3+}. By effectively transmitting energy to Tb^{3+}, Bi^{3+} acts as a sensitizer, increasing excitation efficiency in the 300–400 nm region. There is a great chance that the excitation spectra of Y_2O_3: Bi^{3+} and Y_2O_3:(Tb^{3+}, Bi^{3+}) will be used in UV-LED-pumped white solid-state illumination. Warm-white light emission is indicated by the matching correlated color temperatures of 6689 K and 6875 K. These findings imply that Bi^{3+} co-doped Y_2O_3:Tb^{3+} phosphors are good options for warm -white components needed in near-UV-excited white LEDs.

References

1. Ropp R. C. (2004) Luminescence and the Solid State. Elsevier.
2. Som S. *et al.* (2015) Synthesis of strong red-emitting Y_2O_3: Eu^{3+} phosphor by chemical routes: structural evolution, photometric properties, and Judd–Ofelt analysis. RSC Advances, 5, 70887-70898.
3. Chen J. et al. (2008) Hydrothermal synthesis of ordered Y_2O_3:Eu^{3+} nanolamella architectures and their luminescent properties. Physica E: Low-Dimensional Systems and Nanostructures, 41, 304–308.
4. Chi L.S. et al. (2005) Synthesis of Y_2O_3:Eu, Bi red phosphors by homogeneous co-precipitation and their photoluminescence behaviors. Journal of The Electrochemical Society, 152, J93.
5. Zhang H. et al. (2015) Strategies for boosting phosphor luminescence efficiency via energy transfer. Chemical Society Reviews, 44, 362–376.
6. Yu R. et al. (2009) Structural and luminescent properties of Bi-doped Y_2O_3:Tb^{3+} phosphors. Materials Letters, 63, 2212–2214.
7. Yen W.M. et al. (2004) Inorganic Phosphors: Compositions, Preparation and Optical Properties. CRC Press, 496.
8. Gupta S.K., *et al.* (2014) Structural and photoluminescence properties of Y_2O_3:Tb^{3+} nanophosphors. Journal of Luminescence, 145, 828–834.
9. Wen X., *et al.* (2010) Synthesis and luminescent properties of Tb^{3+}-doped Y_2O_3 nanophosphors via hydrothermal method. Journal of Rare Earths, 28, 903–907.
10. Wang F., *et al.* (2010) Lanthanide-doped nanocrystals as luminescent probes for bioimaging. Chemical Society Reviews, 39, 1294–1308.
11. F. et al. (2021) Synthesis, characterization and radioluminescence properties of erbium-doped yttria phosphors, International Journal of Minerals, Metallurgy and Materials, 28, 1983–1990.
12. Wang Y. et al. (2002) Synthesis and luminescence of Y_2O_3:Tb nanocrystals. Journal of Materials Chemistry, 12, 1239–1241.
13. Aruna S.T. et al. (2008) Combustion synthesis and nanomaterials. Current Opinion in Solid State and Materials Science, 12, 44–50.
14. Chen G. et al. (2011). Enhanced luminescence in Bi^{3+}/rare-earth-doped Y_2O_3 nanophosphors. Optical Materials, 33, 881–886.
15. Xu X. et al. (2008). Energy transfer from Bi^{3+} to Tb^{3+} in Bi^{3+}/Tb^{3+} co-doped phosphors. Journal of Alloys and Compounds, 456, 280–284.
16. Chauhan V. et al. (2021). Bi^{3+}-assisted luminescence in $SrMoO_4$: Sm^{3+} red phosphor. Journal of Rare Earths, 39, 1336-1343.

17. Chen Z., et al. (2009). Microwave-induced solution combustion synthesis of nano-sized phosphors. Journal of Alloys and Compounds, 473, 13–16.

18. Singh P. et al. (2008). In situ high temperature XRD studies of ZnO nanopowder prepared via cost effective ultrasonic mist chemical vapour deposition**.** Bulletin of Materials Science, 31,573-577.

19. Lin-li, Z., Chang-xin, G., Jun-jing, Z., & Jun-tao, H. (2005) Photoluminescence of Eu(III)-Doped ZnO Nanopowder and Energy Transfer from ZnO to Eu(III) Ions. Chinese Physics Letters,22,1225.

20. Pavitra E. et al. (2012) A novel strategy for controllable emissions from Eu^{3+} or Sm^{3+} ions co-doped $SrY_2O_4:Tb^{3+}$ phosphors. Physical Chemistry Chemical Physics, 14, 11296–11307.

21. Atuchin V.V. et al. (2014) Synthesis and spectroscopic properties of multiferroic β′-$Tb_2(MoO_4)_3$. Optical Materials, 36, 1631–1635.

22. De Oliveira R.S. et al. (2017) Tunable photoluminescence of nanostructured $LaPO_4:Eu^{3+}/Tb^{3+}$ synthesized via a microwave-assisted ethylene glycol route. Ceramics International, 43, 8276–8283.

23. Taikar D.R. et al. (2020). Study of energy transfer from Bi^{3+} to Tb^{3+} in Y_2O_3 phosphor and its application for W-LED. Journal of Alloys and Compounds. 828, 154405

24. Guyot, Y. et al. (2016). Assignment of Yb^{3+} energy levels in the C_2 and C_{3i} centers of Lu_2O_3 sesquioxide. Journal of Luminescence, 170, 513–519.

25. Som S.K. et al. (2013). Influences of doping and annealing on the structural and photoluminescence properties of Y_2O_3 nanophosphors. Journal of Fluorescence, 23, 439–450.

26. Luis M.B. et al. (2018) Luminescent and structural analysis of yttrium oxide doped with different percentages of terbium and dysprosium, to obtain different shades of green to yellow.Journal of Nanophotonics, 12, 026018.

27. Masumoto K. et al. (2011) Luminescence characteristics and annealing effects of Tb-doped AlBNO films for inorganic electroluminescence devices. Japanese Journal of Applied Physics, 50, 4S.

28. Jafer R.M. et al. (2015) X-ray photoelectron spectroscopy and luminescent properties of Y_2O_3: Bi^{3+} phosphor. Applied Surface Science, 332 198-204.